

Weaker Atlantic overturning circulation increases the vulnerability of northern Amazon forests

Received: 30 April 2023

Accepted: 24 September 2024

Published online: 1 November 2024

 Check for updates

T. K. Akabane ¹✉, C. M. Chiessi ², M. Hirota ³, I. Bouimetarhan ⁴, M. Prange ⁵, S. Mulitza ⁵, D. J. Bertassoli Jr¹, C. Häggi ^{6,7}, A. Staal⁸, G. Lohmann ⁹, N. Boers ^{10,11,12}, A. L. Daniau ¹³, R. S. Oliveira ¹⁴, M. C. Campos ^{1,15}, X. Shi ¹⁶ & P. E. De Oliveira^{1,17}

The Atlantic meridional overturning circulation (AMOC) and the Amazon forest are viewed as connected tipping elements in a warming climate system. If global warming exceeds a critical threshold, the AMOC may slow down substantially, changing atmospheric circulation and leading to Amazonia becoming drier in the north and wetter in the south. Yet, the impact of an AMOC slowdown on Amazon vegetation is still not well constrained. Here we use pollen and microcharcoal data from a marine sediment core to assess changes in Amazon vegetation from 25,000 to 12,500 years ago. Additionally, we model vegetation responses to an AMOC slowdown under both glacial and pre-industrial conditions. During a past AMOC slowdown (Heinrich Stadial 1–18,000 to 14,800 years ago), pollen data evidence a decline in cold- and moist-affinity elements, coupled with a rise in seasonal tropical vegetation. This pattern is consistent with the decline in suitability of northern Amazon moist forests in a model with an imposed 50% AMOC weakening under glacial conditions. Our modelling results suggest similar changes for a comparable AMOC slowdown under pre-industrial conditions. Combined with current disturbances such as deforestation and wildfires elsewhere in the basin, an AMOC slowdown may exert a systemic impact on the Amazon forest.

The Amazon is the most species-rich terrestrial ecosystem and the world's largest rainforest, which makes it a crucial biodiversity hotspot and carbon pool¹. Although the Amazon rainforest was mostly resilient to natural climate variability in the past hundreds of thousands of years², the combined effects of deforestation and anthropogenic climate change pose an unprecedented threat to its sustainability³. Specifically, crossing of a tipping point of climate change or deforestation could induce a dieback of the Amazon rainforest, that is, a self-propelled response of vegetation in which large moist forest areas would be replaced by seasonal tropical vegetation types (that is, savannahs and seasonal forests)^{3–5}. Moreover, other tipping elements of

the climate system could cause domino-type cascades (for example, intensification of the El Niño/Southern Oscillation), increasing the risks to the Amazon rainforest^{5,6}.

An anomalous increase in meltwater input to the North Atlantic related to the global warming-induced decline of the Greenland Ice Sheet, for instance, may weaken the Atlantic meridional overturning circulation (AMOC)^{6–9}. This would decrease the northward oceanic heat transport⁹, which, in turn, would shift the tropical rain belt southward^{10,11}. Although uncertainties related to a recent AMOC decline exist^{12,13}, a future weakening of this oceanic circulation system^{7,8,14} may adversely affect the Amazon rainforest by changing rainfall regimes

A full list of affiliations appears at the end of the paper. ✉e-mail: thomask.akabane@gmail.com

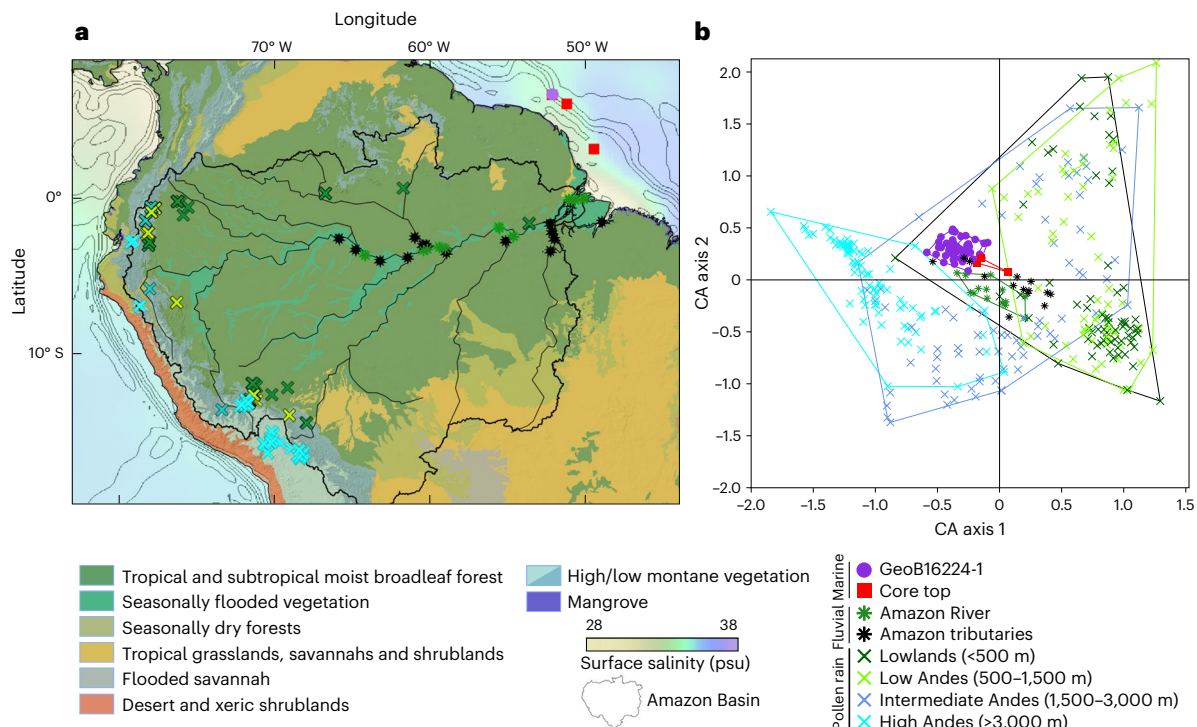


Fig. 1 | Study region and representativity of the marine pollen spectra.

a, Location of the herein studied marine sediment cores (violet circle GeoB16224-1; red squares GeoB16223-1, GeoB16217-2 and GeoB16212-3) and other data used in the correspondence analysis, including riverbed sediment samples from the Amazonian lowlands to the high Andes (crosses)²⁵. The location of the marine core GeoB16224-1 and the superficial marine sample GeoB16223-1 nearly

overlap. The map also depicts the Amazon basin drainage system, ecoregions⁵⁴ and sea surface salinity expressed as practical salinity units (psu)⁵⁵. Ocean bathymetry is shown in 1,000-m intervals. **b**, Correspondence analysis of marine and continental Amazonian pollen signals after removing mangrove taxa and Cyperaceae. We also removed singletons and taxa with less than 5% abundance, *Cecropia* and aquatic taxa. Further details in Supplementary Discussion.

over the northern sector of the basin^{9,11} in addition to the increasing anthropogenic pressures concentrated in its southern and eastern sectors^{15–18}.

Proxy data evidence show that during the last glacial and subsequent deglaciation, phases of AMOC slowdown associated with Heinrich stadials indeed produced southward shifts of the tropical rain belt^{19,20}. This yielded a prolonged dry season in northern Amazonia and increased humidity in its southern regions^{20,21}. Nevertheless, the net total precipitation across the Amazon basin did not change substantially during Heinrich stadials due to the approximately equatorial-centred position of the catchment area²² (Figs. 1 and 2d). Future projections suggest that similar hydrological changes may occur under global warming scenarios^{9,10,23}. It is thus essential to understand how a weakened AMOC has affected Amazonian ecosystems in the past.

Here we present a key high-temporal resolution (about 270 years between data points) Amazonian palynological record that continuously covers the interval from 25,000 to 12,500 calibrated years before present (yr BP), including the Last Glacial Maximum (LGM; 23,000–19,000 yr BP) and Heinrich Stadial 1 (HS1; 18,000–14,800 yr BP) (Fig. 1). The record is based on the well-dated marine sediment core GeoB16224-1 (Extended Data Fig. 1), collected off the Amazon River mouth. This marine core archived Amazonian-sourced organic terrigenous material transported to the ocean by the Amazon River²² (Methods) (Fig. 1). The pollen composition of the analysed marine sediments exhibits a balanced representation of the Amazonian vegetation spectrum^{24,25}, supporting the applicability of our downcore data to interpret changes within the basin (Fig. 1, Extended Data Fig. 2 and Supplementary Discussion). In addition, we use climate and tropical moist forest distribution modelling to assess the most vulnerable Amazonian regions to AMOC slowdown scenarios. Here warm-tropical

forests are represented by rainforests, seasonal tropical forests and floodplain forests, whereas montane forests are treated separately.

Amazonia during the LGM

The LGM environmental conditions shaped Amazonian ecosystems by shifting plant populations and rearranging communities and vegetation types^{21,26–28}. During this period, atmospheric CO₂ concentrations were about 100–120 ppm lower than pre-industrial Holocene levels²⁹. Precipitation decreased in the eastern and central Amazonia^{22,30} but remained high in the western sector of the basin³¹. Meanwhile, mean annual Amazonian temperatures were 4–6 °C lower than pre-industrial Holocene values²⁶. Our basin-integrating pollen data (Fig. 1) indicate that, as consequence, cold-affinity evergreen taxa such as *Podocarpus* and *Hedyosmum* greatly expanded towards the lowlands (Fig. 2k), forming communities alongside lowland elements such as *Alchornea*, *Euterpe*, Melastomataceae, Moraceae, Myrtaceae and *Ilex* (Extended Data Fig. 3). This suggests a widespread shift in the distribution of plant populations. Our record is supported by data from the northern, western and southeastern margins of the basin, where the expansion of *Podocarpus* and other currently montane taxa into lowland Amazonian forests has also been observed during the LGM^{21,26}. These late-Pleistocene forests with no modern analogue sustained a dominant tree cover over most of the basin (Fig. 2e and Extended Data Fig. 4c) but probably with a less-dense structure²⁸. Moreover, the combination of drier conditions³⁰ with lower atmospheric CO₂ concentrations²⁹ also constrained the extent of rainforests^{28,32} (Fig. 2j).

The contrasting trends in cold montane and warm lowland taxa are also highlighted by the Correspondence Analysis (CA), an ordination method that is used to reveal trends of variation in the composition of assemblages. The CA axis 1, which contains the highest relative share of the variability (11.3%) within the dataset, indicates a progressive

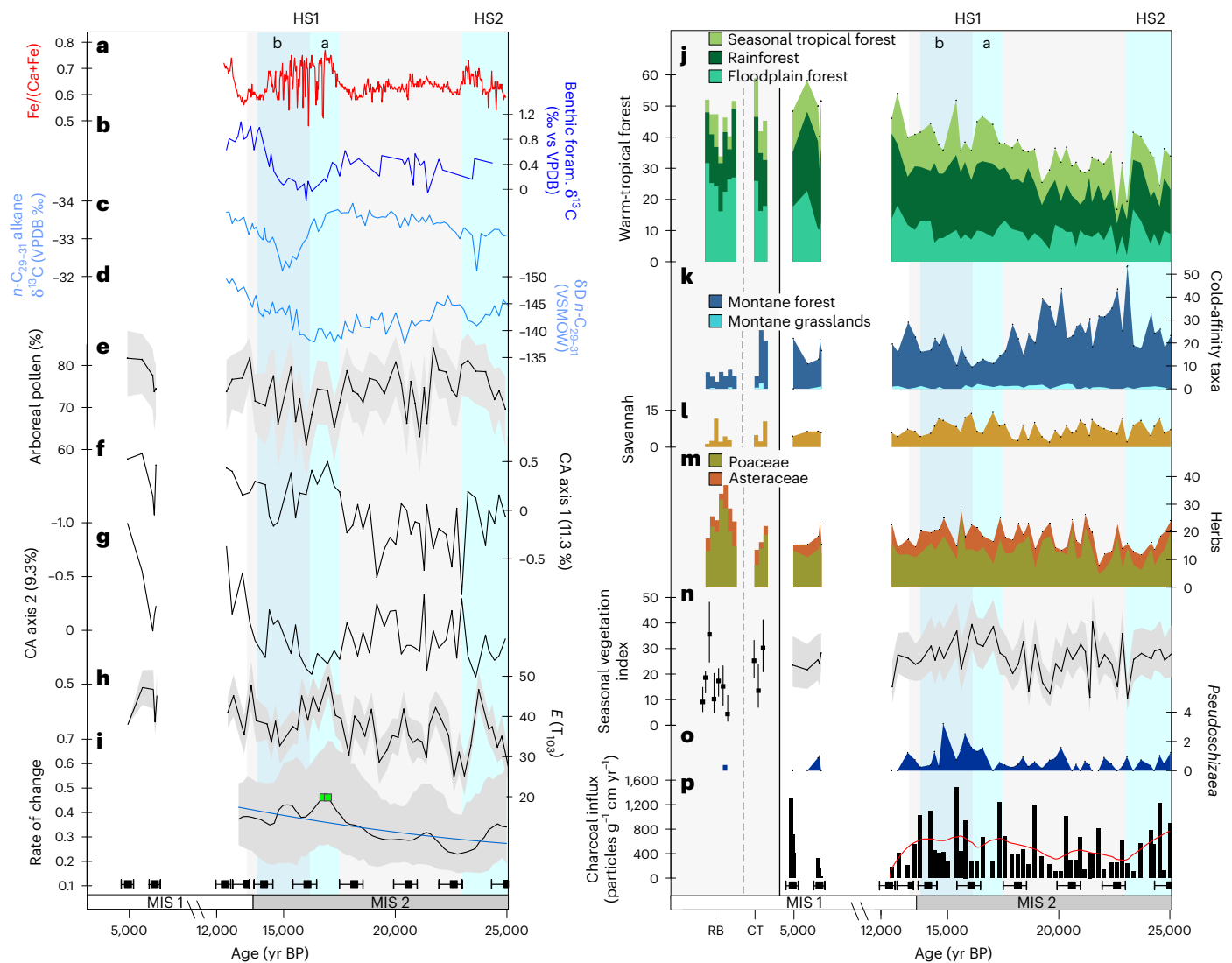


Fig. 2 | Amazonian and equatorial Atlantic environmental changes assessed through data from marine sediment core GeoB16224-1. a, $\text{Fe}/(\text{Fe} + \text{Ca})^{20}$. **b**, Benthic foraminiferal (foram.) stable carbon isotopes ($\delta^{13}\text{C}^{36}$). **c, d**, Plant-waxes $\delta^{13}\text{C}_{n\text{-C}_{29-31}}$ (**c**) and $\delta\text{D}_{n\text{-C}_{29-31}}$ (**d**). **e**, Arboreal pollen (%). **f, g**, Correspondence analysis (CA) axis 1 (**f**) and axis 2 (**g**). **h**, Richness estimation through rarefaction for 82 pollen counts $E(T_{82})$. **i**, Rate-of-change curve with peak points associated to accelerated changes in composition or relative abundances (green squares). **j–m**, Percentages of pollen groups and the respective main taxa: warm-tropical forests subdivided in seasonal tropical forest (Myrtaceae, *Banisteriopsis*, *Euplassa*, *Roupala*, *Piper*, *Solanum*, *Tabebuia*, *Astronium*), rainforest (Melastomataceae, *Euterpe*, *Ilex*, *Moraceae*, *Protium*, *Malpighiaceae*, *Schefflera*) and floodplain forest (*Alchornea*, *Mauritia*, *Sloanea*, *Virola*, *Pouteria*, *Sapium*, *Symmeria*) (**j**); cold-affinity taxa subdivided in montane forests (*Podocarpus*, *Hedyosmum*, *Alnus*, *Ericaceae*, *Myrica*, *Myrsine*) and grasslands (*Brassicaceae*, *Iresine*, *Ribes*, *Juglans*, *Ephedra*) (**k**); savannah (*Borreria*, *Gomphrena*, *Alternanthera*, *Lippia*, *Mimosa*, *Crotalaria*,

Heliotropium) (**l**) and contribution of Poaceae and Asteraceae (**m**). **n**, Seasonal vegetation index: relative contribution of savannah and seasonal forest by the total of defined vegetation types. **o**, Algae spore *Pseudoschizaea*. **p**, Microcharcoal influx is shown by black bars, with a LOESS fit represented by the red line. **e, h, i, n**, 95% confidence interval represented by grey areas and bars. RB: riverbed sediments shown in Fig. 1; CT: core-top samples from marine sediment cores GeoB16212-3, GeoB16217-3 and GeoB16223-1. Marine Isotope Stages (MIS) and Heinrich Stadials (HS) are indicated, with phases 'a' and 'b' of Heinrich Stadial I specifically depicted. Bottom black squares and bars represent radiocarbon-calibrated ages and their respective errors expressed as calibrated years before present (yr BP). The break in the x-axis between about 12,500 and 6,200 yr cal BP represents a hiatus. The solid vertical line distinguishes samples from the marine sediment core GeoB16224-1 from those representing more recent settings, including CT and RB, which are separated by a dashed vertical line. VPDB, Vienna Pee Dee Belemnite standard; VSMOW, Vienna Standard Mean Ocean Water standard.

increase of tropical forests from about 20,000 yr BP towards the Holocene (Fig. 2f,j). Most of the taxa substantially controlling positive values of CA axis 1 (Fig. 2f and Supplementary Table 1) are associated to the warm-tropical forests, that is, *Alchornea*, *Anacardiaceae*, *Sloanea*, *Cupania*, *Moraceae*, *Piper* and *Euterpe*. On the other hand, the negative values of CA axis 1 are predominantly driven by the cold-affinity *Podocarpus* (Fig. 2f and Supplementary Table 1). The progressive replacement of montane (negative CA values) by lowlands (positive CA values) related taxa depicted by the main CA axis suggests that most long-term floristic shifts within the Amazon basin occurred due

to rising temperatures and atmospheric CO_2 concentrations after the LGM (Fig. 2f,j and Extended Data Fig. 5).

The dominant presence of tropical moist and cold-affinity forest taxa, together with high arboreal pollen contribution and weakened fire activity during the LGM (Fig. 2e,j,k,p) challenges the view of a major LGM savannah expansion crossing through the entire central-eastern Amazon basin³³. In that scenario, a substantial replacement of forest by savannah taxa and a substantial increase of herbs would be expected during the LGM in our record because the pollen load transported throughout the Amazon River is influenced by downstream

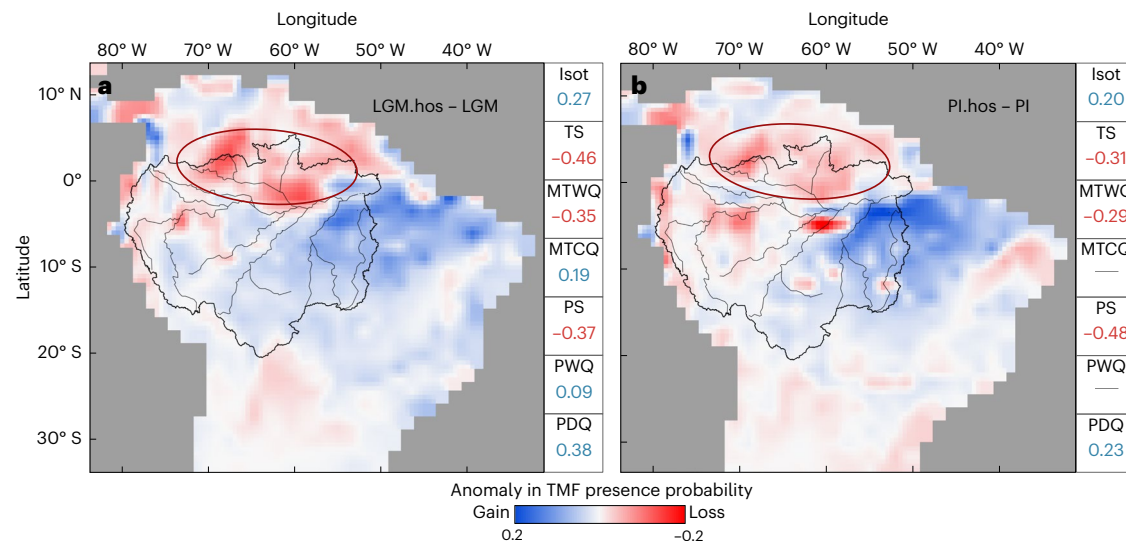


Fig. 3 | Anomalies in the suitability of tropical moist forests over South America. **a, b**, Heinrich Stadial 1 (LGM.hos) minus LGM (**a**) and pre-industrial with an AMOC slowdown (PI.hos) minus pre-industrial (PI) (**b**). Scenario **a** depicts a weakening of the AMOC from 12 to 6 Sv, whereas scenario **b** a weakening from 18 to 9 Sv. The suitability of tropical moist forests (TMF) was calculated for the different scenarios based on the MaxEnt algorithm and bioclimatic parameters extracted from the atmosphere–ocean general circulation model CCSM3⁴⁸. Each panel also shows the Spearman correlation coefficients ($\rho < 0.05$; blue

for positive and red for negative values) calculated between the anomalies of TMF suitability and the anomalies of selected bioclimatic parameters (Isot: isothermality; TS: temperature seasonality; MTWQ: mean temperature of warmest quarter; MTCQ: mean temperature of coldest quarter; PS: precipitation seasonality; PWQ: precipitation of wettest quarter; PDQ: precipitation of driest quarter). Red ellipse indicates the most vulnerable parts of northern Amazonia for the projected scenarios.

river stretches of the Amazonian lowlands²⁴. Instead, we argue that forests dominated the late-Pleistocene Amazon basin, sustained in part by the lower temperatures and expansion of currently montane tree taxa (Fig. 2e,k). Vegetation opening during the LGM was probably concentrated at the margins of the Amazon basin, as recorded in the southern²⁷, eastern²¹ and northern³⁴ Amazonian ecotones and simulated by our vegetation model (Extended Data Fig. 4c). This marginal expansion of dry-affinity taxa and open physiognomies^{21,27,28} is reflected in our record by slightly higher-than-Holocene presence of savannah taxa during the LGM (Fig. 2l). Importantly, savannah taxa encompass ruderal herbs (for example, *Borreria*, *Heliotropium*, *Crotalaria*), which may also represent vegetation disturbances rather than strictly indicating changes in biome.

Heinrich Stadial 1 AMOC slowdown

The weakening of the AMOC during HSI³⁵ is prominently recorded in our sediment core by a marked decrease in deep-sea ventilation (that is, more negative values of benthic foraminiferal stable carbon isotopes, $\delta^{13}\text{C}$)³⁶ (Fig. 2b). Synchronous with the AMOC weakening, a southward displacement of the tropical rain belt^{37,38} induced drier conditions in northern South America^{19,34,39}, whereas precipitation increased in western³¹ and eastern³⁰ Amazonian sectors. In our marine sediment core, the increase in terrigenous input indices such as $\text{Fe}/(\text{Fe}+\text{Ca})$ ²² (Fig. 2a) and branched and isoprenoid tetraether values and the decrease in C_{32} 1,15 long-chain alkyl diol, a proxy for freshwater primary productivity and less turbid waters, point to a higher sediment discharge to the western equatorial Atlantic by the Amazon River⁴⁰. However, despite important shifts in the main precipitation locus during the HSI, net precipitation showed only an increasing trend after about 16,900 yr BP (refs. 22,41) (Fig. 2d).

Our palynological data show changes at the very beginning of HSIa (18,000–16,900 yr BP) (Fig. 2e–o and Extended Data Fig. 3), unlike the plant wax $\delta^{13}\text{C}$ record from the same core²² (Fig. 2c). At the onset of HSIa, taxa related to the warm-tropical forests and savannahs expanded as cold-affinity taxa retreated (Fig. 2j,k,l) led by changes in rainfall patterns. This period is also marked by oscillations in the arboreal

pollen percentages towards lower values (Fig. 2e). In general, there is a relative expansion of savannah and seasonal forests in comparison to evergreen forests (both montane and lowland tropical forests) (Fig. 2n). This pattern is revealed by the higher values of the seasonal vegetation index (Fig. 2n), which represents the proportion of savannah and seasonal vegetation taxa relative to other vegetation categories. The decrease of *Podocarpus*, a drought-intolerant and cold-affinity conifer, along with that of *Hedyosmum* (Fig. 2k) suggests a localized loss of suitability of late-Pleistocene tropical forests. This scenario is supported by our model results based on ~50% AMOC weakening under LGM boundary conditions (from 12 to 6 Sv) (Fig. 3a). These representatives of the modern montane forests widely integrated the lowlands, probably concentrated at the northern and western parts of the basin spreading from the Andes and from the Guyana highlands^{42,43} (Fig. 1). This loss was probably caused by a combination of gradually rising global temperatures and abruptly localized precipitation reduction in northern Amazonia (Fig. 3a). The peak in compositional change (Fig. 2i) at HSIa indicates a short-term change in precipitation might have been the primary factor, whereas temperature-moderated trends were more gradual as demonstrated in CA axis 1 (Fig. 2f). The initial HSIa increase of warm-tropical forest taxa probably represents its expansion over the eastern and southeastern parts of the basin, or its relative increase, alongside with savannahs, to the detriment of mixed forests (Extended Data Fig. 4d).

At the HSIa, the increase in palynological richness (Fig. 2h) led by a higher diversity of savannah and seasonal tropical forest taxa suggests an increase in vegetation mosaics and boundaries within the catchment area. This is supported by the synchronous CA axis 2 negative incursion, mainly driven by taxa such as Melastomataceae, Myrtaceae, *Borreria*, Asteraceae, *Gomphrena*, *Alternanthera*, *Myrsine* and *Byrsonima* (Fig. 2g and Supplementary Table 1), some of which can be associated to higher seasonality and open vegetation physiognomies. Moreover, conspicuous correlations of the CA axis 2 and the seasonal vegetation index with precipitation, as recorded by δD ²² (Fig. 2d,g,n and Extended Data Fig. 5), indicate that slightly drier conditions were sufficient to drive changes in vegetation composition. This vegetation turnover probably

took place in the northern sector of the Amazon basin as supported by our model results (Fig. 3a). The anomaly in the distribution of tropical moist forests from the LGM to HS1 over northern Amazonia (Fig. 3a) suggests a loss of their suitability, driven by reduced precipitation and higher seasonality. Furthermore, data from the Cariaco basin indicate an expansion of drier vegetation in northernmost South America within a few decades of the onset of stadials⁴³.

The HS1b (about 16,900–14,800 yr BP) marks the maximum and most prolonged southward displacement of the tropical rain belt¹⁹ (Extended Data Fig. 5b). Likewise, maximum moisture availability and forest extent occurred in northeastern Brazil⁴⁴ to the southeast of the Amazonia (Extended Data Fig. 4d). This period also coincides with the re-expansion of *Podocarpus* in southeastern Amazonia^{21,45} and was recorded in our core (Fig. 2k). However, a substantial part of this forest expansion took place outside of the drainage limits⁴⁴, whereas the northern sector of the Amazon basin remained exposed to higher seasonality^{34,39}. Our data show increased fire activity and high relative contribution of seasonal tropical vegetation types during the transition from HS1a to HS1b at about 16,900 yr BP (Fig. 2n,p), coeval to the weakest phase of the AMOC³⁶ (Fig. 2b). These changes are probably linked to the loss of suitable forest habitats over northern Amazonia linked to relatively drier conditions over these areas⁴⁶ (Fig. 3a).

Towards the end of the HS1b, net precipitation over the basin increased (Fig. 2c) along with freshwater discharge by the Amazon River, as recorded by a decrease in sea surface salinity^{22,41} and higher input of the algal spore *Pseudoschizaea* (Fig. 2o). Moreover, the decline in terrigenous sediment supply that characterized HS1b in relation to HS1a (Fig. 2a) was related to a shift of the main precipitation locus from the Andes towards the central and eastern parts of the Amazonian lowlands⁴¹. These changes in rainfall patterns, probably favoured the recruitment of wet-affinity taxa over areas previously exposed to higher seasonality, as shown by the decrease in the seasonal vegetation index (Fig. 2m and Extended Data Fig. 5). Changes in sediment supply might have been responsible for a slight HS1 decreasing trend in floodplain forests (Fig. 2j) due to an accelerated incision of riverine channels. In fact, the contribution of floodplain forests remained low through the glacial period, gradually increasing towards the Holocene when the highest values are achieved, a trend that aligns with the expansion of seasonally flooded environments in response to the rising sea levels⁴⁷ (Fig. 2j).

The recurrence of periods of increased seasonality in the northern parts of the Amazon basin such as HS1 over the Quaternary may explain some of the modern spatial patterns of Amazonian vegetation diversity and structure. In particular, the southern and northern Amazonian forests are consistently less diverse and have lower tree density than the forests occurring in the western and central sectors, which cannot be solely attributed to modern rainfall patterns⁴⁸. In addition, a cyclic connectivity of currently discontinuous patches of savannahs in northern Amazonia during Heinrich stadials probably allowed biotic exchange and gene flow over these areas (Extended Data Fig. 4d). Instead of a large replacement of forests by savannahs, a stepwise connectiveness²² of open vegetation enclaves (Extended Data Fig. 4c,d) or a higher permeability of the late-Pleistocene tropical forests with lower canopy density²⁸ could have allowed a higher dispersion of species that are currently isolated by the surrounding dense rainforests.

AMOC slowdown projection

The herein characterized response of the Amazonian vegetation to a past AMOC slowdown provides key insights into the mechanistic links between these two pivotal tipping elements of Earth's system⁶. To further investigate the effects of an AMOC slowdown to the Amazon forest under a warmer interglacial scenario, we performed a freshwater hosing experiment with the CCSM3 climate model⁴⁹ using pre-industrial boundary conditions. We used a 50% weakening of the AMOC, from about 18 to 9 Sv, which is in the same order of magnitude

as most projections for the end of this century^{50,51}. We then performed distribution modelling for tropical moist forests under (1) pre-industrial and (2) pre-industrial with AMOC slowdown scenarios (Fig. 3b). In such scenarios, we find similar vegetation anomalies as those recorded from the LGM to HS1 (Fig. 3). The projected loss of tropical moist forest habitat suitability in both the HS1 and the pre-industrial AMOC slowdown experiments are significantly correlated to increased seasonality in precipitation and temperature (Fig. 3). In our experiments, the magnitude of AMOC weakening and the resulting decrease in mean precipitation and increase in seasonality over northern Amazonia are similar to the changes observed from ensemble simulations of AMOC decline due to an abrupt fourfold increase in CO₂ from the Coupled Model Intercomparison Project phases 5 (CMIP5) and 6 (CMIP6)²³. These regions are also pointed as vulnerable under rising global temperatures by CMIP6 models⁵².

Within an AMOC slowdown scenario, an intensification of seasonality coupled with reduced annual precipitation²³ may introduce additional ecosystem stress on the northern Amazonia (Fig. 3b). Similar changes in the past led to localized northern encroachment of seasonal tropical vegetation whereas, in theory, a future southward displacement of the tropical rain belt should stabilize the southern and eastern Amazon rainforests¹⁰. However, these regions that could potentially benefit from stabilization also overlap with the already degraded lands at the growing 'arc of deforestation'^{15–18}. Thus, with a business-as-usual scenario, the anticipated north–south shrinkage of Amazon rainforests could accelerate its change into a net carbon source¹⁸ with impacts on global carbon and hydrological cycles.

Our finding that past shifts in precipitation promoted a dry-affinity vegetation composition and some intensification of fire regime (Fig. 2g,n,p) is also in line with modern observations⁵³. Whereas past changes were linked to northern Amazonia due to the AMOC slowdown, the ongoing gradual recruitment of drought-tolerant taxa and increase in mortality of wet-affinity taxa mainly takes place in the historically more degraded eastern Amazonia^{18,53}. Therefore, the negative effects of an AMOC slowdown on the vulnerability of northern Amazonia combined with the current state of anthropogenic pressure over the eastern and southeastern sectors of the basin, could systematically impact the Amazonian ecosystem. Hence, future studies should direct their attention to the combined impacts of potential forthcoming scenarios of AMOC weakening^{7,8} under actual conditions of anthropogenic forest degradation^{15–17} and global warming⁵². Their joint influence could accelerate the approach of Amazonia to a systemic tipping point.

Online content

Any methods, additional references, Nature Portfolio reporting summaries, source data, extended data, supplementary information, acknowledgements, peer review information; details of author contributions and competing interests; and statements of data and code availability are available at <https://doi.org/10.1038/s41561-024-01578-z>.

References

1. Feldpausch, T. R. et al. Tree height integrated into pantropical forest biomass estimates. *Biogeosciences* **9**, 3381–3403 (2012).
2. Kern, A. K. et al. A 1.8 million year history of Amazon vegetation. *Quat. Sci. Rev.* **299**, 107867 (2023).
3. Flores, B. M. et al. Critical transitions in the Amazon forest system. *Nature* **626**, 555–564 (2024).
4. Oliveira, R. S. et al. Linking plant hydraulics and the fast–slow continuum to understand resilience to drought in tropical ecosystems. *N. Phytol.* **230**, 904–923 (2021).
5. Armstrong McKay, D. I. et al. Exceeding 1.5°C global warming could trigger multiple climate tipping points. *Science* **377**, eabn7950 (2022).
6. Wunderling, N. et al. Climate tipping point interactions and cascades: a review. *Earth Syst. Dyn.* **15**, 41–74 (2024).

7. Ditlevsen, P. D. & Ditlevsen, S. Warning of a forthcoming collapse of the Atlantic Meridional Overturning Circulation. *Nat. Commun.* **14**, 4254 (2023).
8. Caesar, L., McCarthy, G. D., Thornalley, D. J. R., Cahill, N. & Rahmstorf, S. Current Atlantic Meridional Overturning Circulation weakest in last millennium. *Nat. Geosci.* **14**, 118–120 (2021).
9. Orihuela-Pinto, B., England, M. H. & Taschetto, A. S. Interbasin and interhemispheric impacts of a collapsed Atlantic overturning circulation. *Nat. Clim. Change* **12**, 558–565 (2022).
10. Nian, D. et al. A potential collapse of the Atlantic Meridional Overturning Circulation may stabilise eastern Amazonian rainforests. *Commun. Earth Environ.* **4**, 470 (2023).
11. Good, P., Boers, N., Boulton, C. A., Lowe, J. A. & Richter, I. How might a collapse in the Atlantic Meridional Overturning Circulation affect rainfall over tropical South America? *Clim. Resil. Sustain.* **1**, e26 (2022).
12. Latif, M., Sun, J., Visbeck, M. & Hadi Bordbar, M. Natural variability has dominated Atlantic Meridional Overturning Circulation since 1900. *Nat. Clim. Change* **12**, 455–460 (2022).
13. Kilbourne, K. H. et al. Atlantic circulation change still uncertain. *Nat. Geosci.* **15**, 165–167 (2022).
14. Boers, N. Observation-based early-warning signals for a collapse of the Atlantic Meridional Overturning Circulation. *Nat. Clim. Change* **11**, 680–688 (2021).
15. Albert, J. S. et al. Human impacts outpace natural processes in the Amazon. *Science* **379**, eabo5003 (2023).
16. Lapola, D. M. et al. The drivers and impacts of Amazon forest degradation. *Science* **379**, eabp8622 (2023).
17. Feng, X. et al. How deregulation, drought and increasing fire impact Amazonian biodiversity. *Nature* **597**, 516–521 (2021).
18. Gatti, L. V. et al. Amazonia as a carbon source linked to deforestation and climate change. *Nature* **595**, 388–393 (2021).
19. Deplazes, G. et al. Links between tropical rainfall and North Atlantic climate during the last glacial period. *Nat. Geosci.* **6**, 213–217 (2013).
20. Zhang, Y. et al. Different precipitation patterns across tropical South America during Heinrich and Dansgaard-Oeschger stadials. *Quat. Sci. Rev.* **177**, 1–9 (2017).
21. Reis, L. S. et al. Hydroclimate and vegetation changes in southeastern Amazonia over the past ~25,000 years. *Quat. Sci. Rev.* **284**, 107466 (2022).
22. Häggi, C. et al. Response of the Amazon rainforest to late pleistocene climate variability. *Earth Planet. Sci. Lett.* **479**, 50–59 (2017).
23. Bellomo, K., Angeloni, M., Corti, S. & von Hardenberg, J. Future climate change shaped by inter-model differences in Atlantic Meridional Overturning Circulation response. *Nat. Commun.* **12**, 3659 (2021).
24. Akabane, T. K. et al. Modern pollen signatures of Amazonian rivers and new insights for environmental reconstructions. *Palaeogeogr. Palaeoclimatol. Palaeoecol.* **554**, 109802 (2020).
25. Bush, M. B. et al. Modern pollen assemblages of the Neotropics. *J. Biogeogr.* **48**, 231–241 (2021).
26. Colinvaux, P. A., De Oliveira, P. E., Moreno, J. E., Miller, M. C. & Bush, M. B. A long pollen record from lowland Amazonia: forest and cooling in glacial times. *Science* **274**, 85–88 (1996).
27. Mayle, F. E., Burbridge, R. & Killeen, T. J. Millennial-scale dynamics of southern Amazonian rain forests. *Science* **290**, 2291–2294 (2000).
28. Cowling, S. A., Maslin, M. A. & Sykes, M. T. Paleovegetation simulations of lowland Amazonia and implications for neotropical allopatry and speciation. *Quat. Res.* **55**, 140–149 (2001).
29. Petit, J. R. et al. Climate and atmospheric history of the past 420,000 years from the Vostok ice core, Antarctica. *Nature* **399**, 429–436 (1999).
30. Wang, X. et al. Hydroclimate changes across the Amazon lowlands over the past 45,000 years. *Nature* **541**, 204–207 (2017).
31. Cheng, H. et al. Climate change patterns in Amazonia and biodiversity. *Nat. Commun.* **4**, 1411 (2013).
32. Maksic, J. et al. Brazilian biomes distribution: past and future. *Palaeogeogr. Palaeoclimatol. Palaeoecol.* **585**, 110717 (2022).
33. Sato, H. et al. Dry corridors opened by fire and low CO₂ in Amazonian rainforest during the last glacial maximum. *Nat. Geosci.* **14**, 578–585 (2021).
34. Zular, A. et al. The role of abrupt climate change in the formation of an open vegetation enclave in northern Amazonia during the late Quaternary. *Glob. Planet. Change* **172**, 140–149 (2019).
35. Pöppelmeier, F., Jeltsch-Thömmes, A., Lippold, J., Joos, F. & Stocker, T. F. Multi-proxy constraints on Atlantic circulation dynamics since the last ice age. *Nat. Geosci.* **16**, 349–356 (2023).
36. Voigt, I. et al. Variability in mid-depth ventilation of the western Atlantic Ocean during the last deglaciation. *Paleoceanography* **32**, 948–965 (2017).
37. Kageyama, M. et al. Climatic impacts of fresh water hosing under last glacial maximum conditions: a multi-model study. *Clim. Past* **9**, 935–953 (2013).
38. Multiza, S. et al. Synchronous and proportional deglacial changes in Atlantic Meridional Overturning and northeast Brazilian precipitation. *Paleoceanography* **32**, 622–633 (2017).
39. Campos, M. C. et al. A new mechanism for millennial scale positive precipitation anomalies over tropical South America. *Quat. Sci. Rev.* **225**, 105990 (2019).
40. Häggi, C. et al. Modern and late Pleistocene particulate organic carbon transport by the Amazon River: insights from long-chain alkyl diols. *Geochim. Cosmochim. Acta* **262**, 1–19 (2019).
41. Crivellari, S. et al. Increased Amazon freshwater discharge during late Heinrich Stadial 1. *Quat. Sci. Rev.* **181**, 144–155 (2018).
42. D’Apolito, C., Absy, M. L. & Latrubesse, E. M. The Hill of Six Lakes revisited: new data and re-evaluation of a key Pleistocene Amazon site. *Quat. Sci. Rev.* **76**, 140–155 (2013).
43. Hughen, K. A., Eglinton, T. I., Xu, L. & Makou, M. Abrupt tropical vegetation response to rapid climate changes. *Science* **304**, 1955–1959 (2004).
44. Dupont, L. M. et al. Two-step vegetation response to enhanced precipitation in Northeast Brazil during Heinrich event 1. *Glob. Change Biol.* **16**, 1647–1660 (2009).
45. Pinaya, J. L. D. et al. Brazilian montane rainforests expansion induced by Heinrich Stadial 1 event. *Sci. Rep.* **9**, 17912 (2019).
46. Blaus, A., Nascimento, M. N., Peterson, L. C., McMichael, C. N. H. & Bush, M. B. Climate, vegetation, and fire, during the last deglaciation in northwestern Amazonia. *Quat. Sci. Rev.* **332**, 108662 (2024).
47. Sawakuchi, A. O. et al. Rainfall and sea level drove the expansion of seasonally flooded habitats and associated bird populations across Amazonia. *Nat. Commun.* **13**, 4945 (2022).
48. ter Steege, H. et al. A spatial model of tree alpha-diversity and tree density for the Amazon. *Biodivers. Conserv.* **12**, 2255–2277 (2003).
49. Collins, W. D. et al. The Community Climate System Model Version 3 (CCSM3). *J. Clim.* **19**, 2122–2143 (2006).
50. Weijer, W., Cheng, W., Garuba, O. A., Hu, A. & Nadiga, B. T. CMIP6 models predict significant 21st century decline of the Atlantic Meridional Overturning Circulation. *Geophys. Res. Lett.* **47**, e2019GL086075 (2020).
51. Bakker, P. et al. Fate of the Atlantic meridional overturning circulation: strong decline under continued warming and Greenland melting. *Geophys. Res. Lett.* **43**, 12,252–12,260 (2016).
52. Parry, I. M., Ritchie, P. D. L. & Cox, P. M. Evidence of localised Amazon rainforest dieback in CMIP6 models. *Earth Syst. Dyn.* **13**, 1667–1675 (2022).

53. Esquivel-Muelbert, A. et al. Compositional response of Amazon forests to climate change. *Glob. Change Biol.* **25**, 39–56 (2019).
54. Olson, D. M. et al. Terrestrial ecoregions of the world: a new map of life on Earth. *Bioscience* **51**, 933–938 (2001).
55. Zweng, M. M. et al. *World Ocean Atlas 2013, Volume 2: Salinity* (NOAA Atlas NESDIS 74, 2013).

Springer Nature or its licensor (e.g. a society or other partner) holds exclusive rights to this article under a publishing agreement with the author(s) or other rightsholder(s); author self-archiving of the accepted manuscript version of this article is solely governed by the terms of such publishing agreement and applicable law.

Publisher's note Springer Nature remains neutral with regard to jurisdictional claims in published maps and institutional affiliations.

© The Author(s), under exclusive licence to Springer Nature Limited 2024

¹Institute of Geosciences, University of São Paulo, São Paulo, Brazil. ²School of Arts, Sciences and Humanities, University of São Paulo, São Paulo, Brazil. ³Department of Physics, Federal University of Santa Catarina, Florianópolis, Brazil. ⁴Faculté des Sciences Appliquées, UIZ-Ibn Zohr University of Agadir, Agadir, Morocco. ⁵MARUM—Center for Marine Environmental Sciences, University of Bremen, Bremen, Germany. ⁶Department of Earth and Planetary Sciences, Geological Institute, ETH Zurich, Zurich, Switzerland. ⁷Intercantonal Laboratory, Schaffhausen, Switzerland. ⁸Copernicus Institute of Sustainable Development, Utrecht University, Utrecht, Netherlands. ⁹AWI—Alfred Wegener Institute, Helmholtz Centre for Polar and Marine Research, Bremerhaven, Germany. ¹⁰Earth System Modelling, School of Engineering and Design, Technical University of Munich, Munich, Germany. ¹¹Potsdam Institute for Climate Impact Research, Potsdam, Germany. ¹²Department of Mathematics and Global Systems Institute, University of Exeter, Exeter, UK. ¹³UMR 5805 EPOC, Université de Bordeaux, CNRS, Bordeaux INP, Pessac, France. ¹⁴Departamento de Biologia Vegetal, Universidade Estadual de Campinas (UNICAMP), Campinas, Brazil. ¹⁵Institute of Geosciences, University of Campinas, Campinas, Brazil. ¹⁶Southern Marine Science and Engineering Guangdong Laboratory (Zhuhai), Zhuhai, China. ¹⁷Keller Science Action Center, The Field Museum of Natural History, Chicago, IL, USA.

✉ e-mail: thomask.akabane@gmail.com

Methods

Marine sediment cores

Marine sediment core GeoB16224-1 (gravity core, 6.65° N, 52.09° W; 2,510 m water depth; 760 cm in length) was retrieved from the continental slope off French Guyana during RV Maria S. Merian cruise MSM20/3⁵⁶ (Fig. 1). The relatively stable and high sedimentation rates (that is, 22 cm kyr⁻¹ in average) recorded in the marine core makes it an ideal archive for high-resolution environmental reconstructions. The organic geochemical signals recorded in core GeoB16224-1 attest the Amazonian source of the organic fraction^{22,40,41,57,58}. In addition, εNd₍₀₎ data (that is, -11.11 to -12.22) indicate an Amazonian source for the siliciclastic fraction^{59,60}. The joint use of terrigenous and benthic foraminiferal-based proxies, as performed in this study, allows assessment of the timing of continental changes associated to changes in marine dynamics. The sample from the marine sediment core GeoB16212-3 represents the uppermost 4 cm of a more proximal core (gravity core, 3.10° N, 49.39° W, 75 m water depth). The upper part of core GeoB16212-3 was deposited between 1996 and 2012 according to parasound measurements of the core site and thereby contains high-resolution Anthropocene sediments⁵⁶. The sample from the marine sediment core GeoB16217-2 (gravity core, 6.07° N, 51.30° W, 2,440 m water depth) represents the uppermost 3.5 cm of sediment. The sample from the marine sediment core GeoB16223-1 (multicore, 6.61° N, 52.12° W, 2,251 m water depth) represents the uppermost 1 cm of sediment. Both samples are likely to represent Holocene deposition indicated by the presence of *Globorotalia menardii*⁵⁶. The marine sediment cores are currently stored in the Bremen Core Repository at MARUM, University of Bremen, Germany.

Age model

We focus on the depth interval between 350 cm (25,030 yr BP) and 68 cm (12,483 yr BP) of core GeoB16224-1, which encompasses the LGM and HS1. The age model of the entire core is based on 15 calibrated radiocarbon (¹⁴C) measurements performed on planktonic foraminifera species *Globigerinoides sacculifer* and/or *Globigerinoides ruber*⁶⁰ spanning from -41,000 to 12,400 yr BP. The ¹⁴C ages and a tie point to the U/Th dated El Condor speleothem record³¹ at 46,830 ± 470 yr BP were used to produce an age model using the 'BACON' R package version 2.5.7⁶¹ and the Marine20 calibration curve^{22,62} (Extended Data Fig. 1). A continuous sedimentation of fine-grained sediments was recorded in the core section below 66 cm core depth (-12,370 yr BP), where a discontinuity occurs. Above the discontinuity, samples close to the ¹⁴C measurements at 6 cm (4,944 yr BP) and 50 cm (6,148 yr BP) were also investigated to provide a Holocene signal.

Palynological analysis

We carried the palynological analysis on 52 samples of 4–5 cm³ resulting in an average temporal resolution of 276 yr per sample in the interval between 25,030 and 12,483 yr BP (Extended Data Fig. 3). One *Lycopodium clavatum* tablet (batch number 414831) was added per sample⁶³. The chemical processing consisted in acid digestion in HCl 10% and HF 40% (ref. 64). The samples were sieved over a 5-μm nylon mesh screen using an ultrasonic bath. The remaining residues were stored in distilled water and mounted as semi-permanent slides in glycerine medium. The palynological count and identification were carried on 40×, 63× and 100× magnifications in a light microscope (Zeiss Lab. A1, AxioCam 305 colour). The identification of pollen grains and spores were based on atlases and published descriptions^{65–73}. Whenever necessary, taxonomical identifications were also compared with the pollen collection of the Laboratory of Micropaleontology–Institute of Geosciences, University of São Paulo. Samples were counted to a minimum of 123 pollen grains with an average of 191 counts per sample. When excluding mangrove/coastal vegetation (*Rhizophora*, *Avicennia*, Cyperaceae, *Amaranthus* and *Crenea*) and aquatic taxa (Alismataceae, *Typha*, *Ludwigia*, Pontederia), counts vary between 84 and 226 with an average of 149 counts

per sample⁷⁴. Pollen percentages were calculated independently of these excluded groups to reduce the coastal and aquatic vegetation signal background. The grouping of pollen taxa was based on the modern fluvial data of the Amazon River drainage basin²⁴ and pollen rain studies^{75–80} (Supplementary Discussion) in addition to modern distributions of plant taxa (GBIF: Global Biodiversity Information Facility, BIEN: Botanical Information and Ecology Network). Fern spores resulted in an average of 170 grains per sample. The percentages of the freshwater algae spore *Pseudoschizaea* is presented relative to the pollen sum. Other freshwater algae such as *Botryococcus* or *Spirogyra* were extremely rare and therefore not included here. The pollen diagram was produced with the 'Rioja' R package⁸¹ (Extended Data Fig. 3).

To produce the correspondence analysis (CA) using the downcore data (Fig. 2), we used the 'FactoMineR' R package⁸² on the relative abundance pollen data, excluding: (1) *Rhizophora*, *Avicennia* and Cyperaceae and aquatic macrophyte taxa, (2) singletons and (3) less than 5% abundant taxa in the whole dataset. For the CA including pollen rain and fluvial pollen data, we also removed *Cecropia* and outliers resulted from modern pollen data dominated by a single taxon (for example, samples containing from 30% up to 95% of *Mauritia*, more than 40% of *Heliocarpus*) (Extended Data Fig. 2).

The rate of change was calculated using the 'R-Ratepol' R package with the age-weighted average smoothing method with five data points and binning with four shifts within 1,000 years moving windows. Differences between working units were calculated with the chi-squared coefficient, and scores are represented as dissimilarity per 1,000 years (ref. 83). Palynological richness was estimated by rarefaction for each sample with a minimum of 103 counts and calculated with the 'vegan' R package⁸⁴.

Microcharcoal analysis

The chemical treatment and slide mounting followed Daniau et al.^{85,86}. Samples of about 0.2 g of dried sediment were chemically treated with HCl 37%, HNO₃ 65% and H₂O₂ 35% in hot water bath, with a later application of HF 70% and HCl 25%. The residue was diluted to 0.1 and filtered onto a cellulose acetate membrane containing nitrocellulose of 0.45 μm porosity and 47 mm in diameter. A portion of the membrane was mounted onto a plexiglass slide with ethyl acetate and polished with aluminium powder of 200 Å. We carried out an automatic scanning of 200 view-fields images per sample at ×500 magnification on a Leica DM6000M using transmitted and reflected light. Each photomicrograph represents 0.0614 mm², resulting in a total scanned surface area of 12.28 mm² per sample. By examining the photomicrographs under both transmitted and reflected light, we were able to differentiate charcoal from other black particles and quantify their abundance⁸⁷.

Climate model

We performed four experiments using the atmosphere–ocean general circulation model CCSM3⁴⁹ in the high-resolution version T85 (1.4° atmosphere transform grid; ocean grid resolution nominal 1°). Besides a pre-industrial (PI) and an LGM time-slice simulation (both following the protocol of the Paleoclimate Modelling Intercomparison Project Phase 2 (details in Erokina et al.⁸⁸), two freshwater hosing experiments branching off from the PI and LGM steady climate states (experiments PI.hos and LGM.hos, respectively) were carried out. In both hosing experiments, 0.2 Sv of freshwater were injected into the northern North Atlantic for 400 years, resulting in a steady-state ~50% weakening of the AMOC (from about 18 to 9 Sv in PI.hos and from about 12 to 6 Sv in LGM.hos). It has been shown in a previous study that experiment LGM.hos provides an accurate simulation of tropical South American precipitation changes during Heinrich Stadial 1³⁹.

Nineteen bioclimatic variables were extracted from the four experiments: PI, PI.hos, LGM and LGM.hos. These follow the definitions in ANUCLIM⁸⁹ and consist of the following: BIO1: Annual Mean Temperature; BIO2: Mean Diurnal Range; BIO3: Isothermality; BIO4: Temperature

Seasonality; BIO5: Max Temperature of Warmest Month; BIO6: Min Temperature of Coldest Month; BIO7: Temperature Annual Range; BIO8: Mean Temperature of Wettest Quarter; BIO9: Mean Temperature of Driest Quarter; BIO10: Mean Temperature of Warmest Quarter; BIO11: Mean Temperature of Coldest Quarter; BIO12: Annual Precipitation; BIO13: Precipitation of Wettest Month; BIO14: Precipitation of Driest Month; BIO15: Precipitation Seasonality; BIO16: Precipitation of Wettest Quarter; BIO17: Precipitation of Driest Quarter; BIO18: Precipitation of Warmest Quarter; BIO19: Precipitation of Coldest Quarter.

Distribution model

We generated distribution models for tropical moist forest for the four modelled climate scenarios (PI, PI.hos, LGM, LGM.hos) applying the MaxEnt⁹⁰ (Extended Data Fig. 4 and Fig. 3). The occurrence dataset of tropical moist forest was generated from 250 randomly distributed data points (maximum of one data point per grid) extracted from the respective biome distribution according to Olson et al.⁵⁴ (Supplementary Table 5). We trained the MaxEnt models with 125 randomly selected data points and used the remaining 125 presence points to test each model. The analysed region of interest was cropped⁹¹ to encompass the current South American tropical moist forest distribution between the latitudes 15.60° N to 33.62° S and longitudes 30.23° W to 83.67° W.

We performed the models using the ‘kuenm’ R package⁹², which allows the testing of a large set of candidate models applying distinct combinations of calibration parameters and climatic datasets. The tested parameters ranged from the standard MaxEnt settings to different combinations of features (linear, quadratic, product, threshold and hinge) and regularization multipliers (0.3 to 1.3 in 0.1 steps). Different arrangements of the 19 bioclimatic variables extracted from the four climate model scenarios were evaluated. These included the full bioclimatic dataset and other six reduced arrangements of bioclimatic variables with Pearson’s correlation coefficient <0.9 (ref. 92). Out of 770 generated models, we evaluated 19 models with ROC p-value < 0.05, training omission for the tenth percentile training <0.1 and $\Delta AIC < 15$, and elected one model by visually comparing the projected tropical moist forest distribution for the PI, LGM and LGM.hos scenarios with the interpreted pollen data for the respective timeframe (Supplementary Table 2).

The final MaxEnt models (Extended Data Fig. 4) were generated with a logistic output, linear and product features, regularization multipliers of 0.7, threshold set to tenth percentile training presence and tenfold bootstrap. In this selected model, the training omission for the tenth percentile training presence is 0.099 and the area under the curve (AUC) is 0.723 ± 0.010 . The tenth percentile training presence indicates a threshold in which values equal to or higher are considered to represent suitable habitats. The bioclimatic variables in decreasing order of contribution to the elected models are: BIO11: mean temperature of coldest quarter (43.9%), BIO15: precipitation seasonality (18.7%), BIO17: precipitation of driest quarter (11.9%), BIO3: isothermality (7.7%), BIO4: temperature seasonality (7.5%), BIO10: mean temperature of warmest quarter (7.2%), and BIO16: precipitation of wettest quarter (3.1%).

Data availability

The new data shown herein are available within the supplementary material and through Pangaea (pollen data: <https://doi.org/10.1594/PANGAEA.968664>, charcoal data: <https://doi.org/10.1594/PANGAEA.968665>).

Code availability

The methodology used in the MaxEnt algorithm⁹⁰ is detailed in the manuscript, including the parameters used for running the algorithm. The analysis is based on published methods^{90–92}, allowing reproducibility of results. The CCSM3 source code is disseminated via the Earth System Grid (ESG). Detailed information on how to access the code can be found at <https://www2.cesm.ucar.edu/models/ccsm3.0>. Any further requests for materials can be addressed to T.K.A. or C.M.C.

References

- Mulitza, S. et al. Response of Amazon Sedimentation to Deforestation, Land Use and Climate Variability Cruise No. MSM 20/3, MARIA S. MERIAN-Berichte, DFG-Senatskommission für Ozeanographie, 86 pp. (2013); https://doi.org/10.2312/cr_msm20_3
- Häggi, C. et al. Origin, transport and deposition of leaf-wax biomarkers in the Amazon basin and the adjacent Atlantic. *Geochim. Cosmochim. Acta* **192**, 149–165 (2016).
- Sun, S. et al. Origin and processing of terrestrial organic carbon in the Amazon system: lignin phenols in river, shelf, and fan sediments. *Biogeosciences* **14**, 2495–2512 (2017).
- Höppner, N., Lucassen, F., Chiessi, C. M., Sawakuchi, A. O. & Kasemann, S. A. Holocene provenance shift of suspended particulate matter in the Amazon River basin. *Quat. Sci. Rev.* **190**, 66–80 (2018).
- Zhang, Y. et al. Origin of increased terrigenous supply to the NE South American continental margin during Heinrich Stadial 1 and the Younger Dryas. *Earth Planet. Sci. Lett.* **432**, 493–500 (2015).
- Blaauw, M. & Christen, J. A. Flexible paleoclimate age-depth models using an autoregressive gamma process. *Bayesian Anal.* **6**, 457–474 (2011).
- Heaton, T. J. et al. Marine20—the marine radiocarbon age calibration Curve (0–55,000 cal BP). *Radiocarbon* **62**, 779–820 (2020).
- Stockmarr, J. Tablets with spores used in absolute pollen analysis. *Pollen et. Spores* **13**, 615–621 (1971).
- Faegri, K. & Iversen, J. *Textbook of Pollen Analysis* (Wiley, 1989).
- Roubik, D. W. & Moreno-Patiño, J. E. *Pollen and Spores of Barro Colorado Island* Vol. 36 (Cambridge University Press, 1991).
- Bush, M. B. & Weng, C. Introducing a new (freeware) tool for palynology. *J. Biogeogr.* **34**, 377–380 (2007).
- e Silva, F. H. M. & de Assis Ribeiro dos Santos, F. Pollen morphology of the shrub and arboreal flora of mangroves of northeastern Brazil. *Wetl. Ecol. Manag.* **17**, 423–443 (2009).
- Colinvaux, P., de Oliveira, P. E. & Patiño, J. E. M. *Amazon Pollen Manual and Atlas Manual/Manual e Atlas Palinológico da Amazônia* (Harwood Academic Publishers, 1999).
- de Souza, C. N., Rezende, A. A. & Gasparino, E. C. Pollen morphology of Bignoniaceae from Brazilian forest fragments and its systematic significance. *Palynology* **43**, 333–347 (2019).
- Fontes, D., Jaramillo, C. & Moreno, J. E. Pollen morphology of the Amacayacu Forest dynamics plot, Western Amazon, Colombia. *Palynology* **44**, 32–79 (2020).
- Heusser, C. J. *Pollen and Spores of Chile* Vol. 98 (Univ. of Arizona Press, 1971).
- Hooghiemstra, H. *Vegetational and Climatic History of the High Plain of Bogota, Colombia: A Continuous Record of 3.5 Million Years (Dissertationes Botanicae)* (Lubrecht & Cramer Ltd, 1984).
- Leal, A., Berrío, J. C., Raimúndez, E. & Bilbao, B. A pollen atlas of premontane woody and herbaceous communities from the upland savannas of Guayana, Venezuela. *Palynology* **35**, 226–266 (2011).
- Akabane, T. K. et al. Pollen counts of sediment core GeoB16224-1 from Amazonia, off French Guyana coast. *Pangaea* <https://doi.org/10.1594/PANGAEA.968664> (2024).
- Bush, M. B. Modern pollen-rain data from South and Central America: a test of the feasibility of fine-resolution lowland tropical palynology. *Holocene* **1**, 162–167 (1991).
- Gosling, W. D., Mayle, F. E., Tate, N. J. & Killeen, T. J. Modern pollen-rain characteristics of tall terra firme moist evergreen forest, southern Amazonia. *Quat. Res.* **64**, 284–297 (2005).
- Gosling, W. D., Mayle, F. E., Tate, N. J. & Killeen, T. J. Differentiation between Neotropical rainforest, dry forest, and savannah ecosystems by their modern pollen spectra and implications for the fossil pollen record. *Rev. Palaeobot. Palynol.* **153**, 70–85 (2009).

78. Burn, M. J., Mayle, F. E. & Killeen, T. J. Pollen-based differentiation of Amazonian rainforest communities and implications for lowland palaeoecology in tropical South America. *Palaeogeogr. Palaeoclimatol. Palaeoecol.* **295**, 1–18 (2010).
79. Absy, M. L., Cleef, A. M., D'Apolito, C. & da Silva, M. F. F. Palynological differentiation of savanna types in Carajás, Brazil (southeastern Amazonia). *Palynology* **38**, 78–89 (2014).
80. Jones, H. T., Mayle, F. E., Pennington, R. T. & Killeen, T. J. Characterisation of Bolivian savanna ecosystems by their modern pollen rain and implications for fossil pollen records. *Rev. Palaeobot. Palynol.* **164**, 223–237 (2011).
81. Juggins, S. Rioja: analysis of quaternary science data. R version 1.0-6. CRAN <https://cran.r-project.org/package=rioja> (2023).
82. Husson, A. F., Josse, J., Le, S., Mazet, J. & Husson, M. F. FactoMineR: a package for multivariate analysis. *J. Stat. Softw.* **25**, 1–18 (2008).
83. Mottl, O. et al. Rate-of-change analysis in paleoecology revisited: a new approach. *Rev. Palaeobot. Palynol.* **293**, 104483 (2021).
84. Oksanen, J. et al. Vegan: community ecology package. R version 2.6-2. CRAN <https://cran.r-project.org/web/packages/vegan/vegan.pdf> (2022).
85. Daniau, A. L. et al. Dansgaard–Oeschger climatic variability revealed by fire emissions in southwestern Iberia. *Quat. Sci. Rev.* **26**, 1369–1383 (2007).
86. Daniau, A. L., Goñi, M. F. S. & Duprat, J. Last glacial fire regime variability in western France inferred from microcharcoal preserved in core MDO4-2845, Bay of Biscay. *Quat. Res.* **71**, 385–396 (2009).
87. Akabane, T. K. et al. Microcharcoal concentration of sediment core GeoB16224-1 from Amazonia, off French Guyana coast. *Pangaea* <https://doi.org/10.1594/PANGAEA.968665> (2024).
88. Erokina, O. et al. Dependence of slope lapse rate over the Greenland ice sheet on background climate. *J. Glaciol.* **63**, 568–572 (2017).
89. Xu, T. & Hutchinson, M. *ANUCLIM Version 6.1 User Guide* (Australian National University, Fenner School of Environment and Society, 2011).
90. Phillips, S. J. & Dudík, M. Modeling of species distributions with Maxent: new extensions and a comprehensive evaluation. *Ecography* **31**, 161–175 (2008).
91. Merow, C., Smith, M. J. & Silander, J. A. A practical guide to MaxEnt for modeling species' distributions: what it does, and why inputs and settings matter. *Ecography* **36**, 1058–1069 (2013).
92. Cobos, M. E., Peterson, A. T., Barve, N. & Osorio-Olvera, L. Kuenm: an R package for detailed development of ecological niche models using Maxent. *PeerJ* **7**, e6281 (2019).
93. Bereiter, B. et al. Revision of the EPICA Dome C CO₂ record from 800 to 600-kyr before present. *Geophys. Res. Lett.* **42**, 542–549 (2015).

Acknowledgements

This work was funded by the State of São Paulo Research Foundation–FAPESP project PPTEAM (grant 2018/15123-4). T.K.A. acknowledges the

financial from FAPESP (grants 2019/19948-0 and 2021/13129-8). C.M.C. acknowledges the financial support from CNPq (grant 312458/2020-7). C.M.C. thanks the CLAMBIO consortium and the BiodivERsA 2019–2020 Joint COFUND Call on 'Biodiversity and Climate Change'. CLAMBIO is partially funded by FAPESP (2019/24349-9). Logistic and technical assistance was provided by the captain and crew of the RV MS Merian. M.C.C. acknowledges the financial support from FAPESP (grant 2019/25179-0). D.J.B. acknowledges the financial support from FAPESP (grants 2019/24977-0 and 2022/06640-1). N.B. acknowledges funding by the Volkswagen foundation and the European Union's Horizon Europe research and innovation programme under grant agreement number 101137601 (ClimTip contribution number 17). We thank M. Georget on laboratory assistance during the microcharcoal analysis. Thanks are also due to the Herbarium staff of the Field Museum of Natural History in Chicago for allowing pollen sampling, which improved our taxonomical identifications.

Author contributions

T.K.A. carried out the palynological analysis and the niche distribution modelling; contributed to the design and discussion and led the writing of the manuscript. C.M.C. conceived the project, provided a substantial contribution to the design and discussions and co-wrote the paper. P.E.D.O. assisted with and provided resources for the palynological analysis and contributed to the interpretation of the data. M.H. contributed to the design and co-wrote the paper. I.B. performed preliminary palynological analysis. M.P. and G.L. provided the climate models. A.L.D. assisted with the microcharcoal analysis. D.J.B. contributed to the interpretations. M.H., I.B., M.P., G.L., D.J.B., C.H., M.C.C., A.S., N.B., R.S.O., A.L.D., X.S. and S.M. contributed to the discussion and critical revision of the paper. All authors read and approved the final manuscript.

Competing interests

The authors declare no competing interests.

Additional information

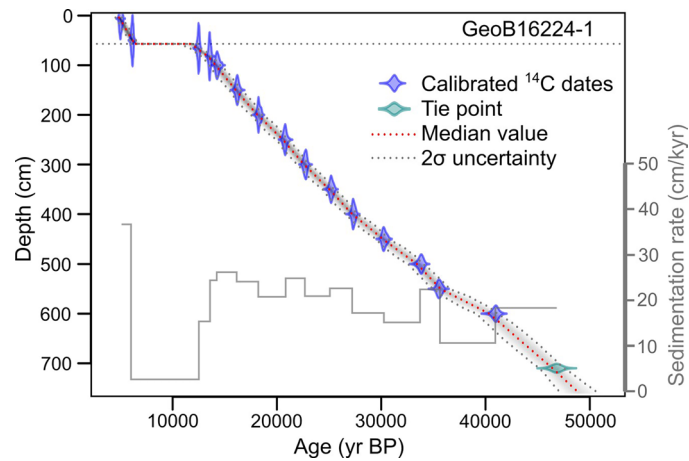
Extended data is available for this paper at <https://doi.org/10.1038/s41561-024-01578-z>.

Supplementary information The online version contains supplementary material available at <https://doi.org/10.1038/s41561-024-01578-z>.

Correspondence and requests for materials should be addressed to T. K. Akabane.

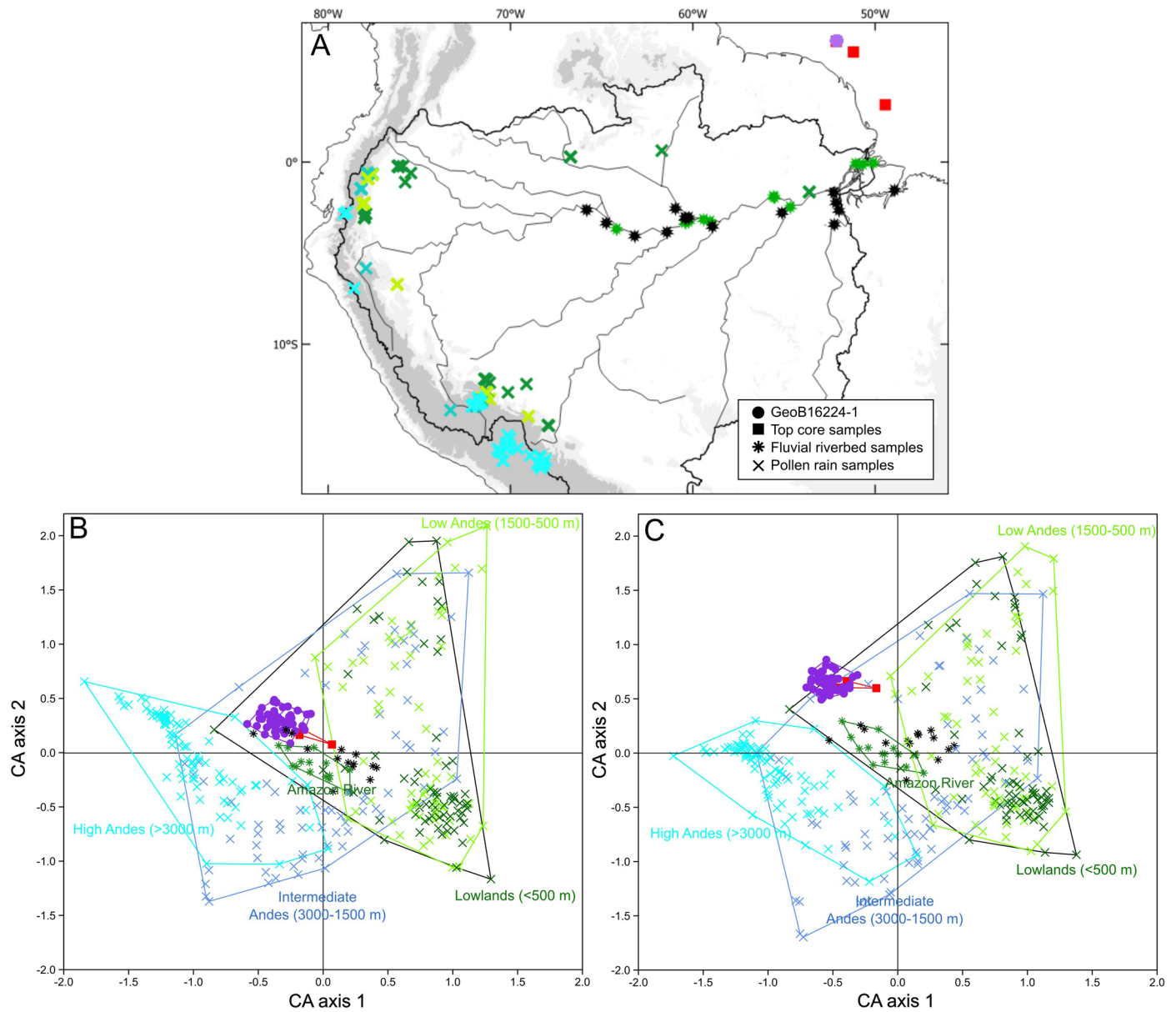
Peer review information *Nature Geoscience* thanks Marcelo Cohen, Alan Wanamaker and Xianfeng Wang for their contribution to the peer review of this work. Primary Handling Editor: James Super, in collaboration with the *Nature Geoscience* team.

Reprints and permissions information is available at www.nature.com/reprints.



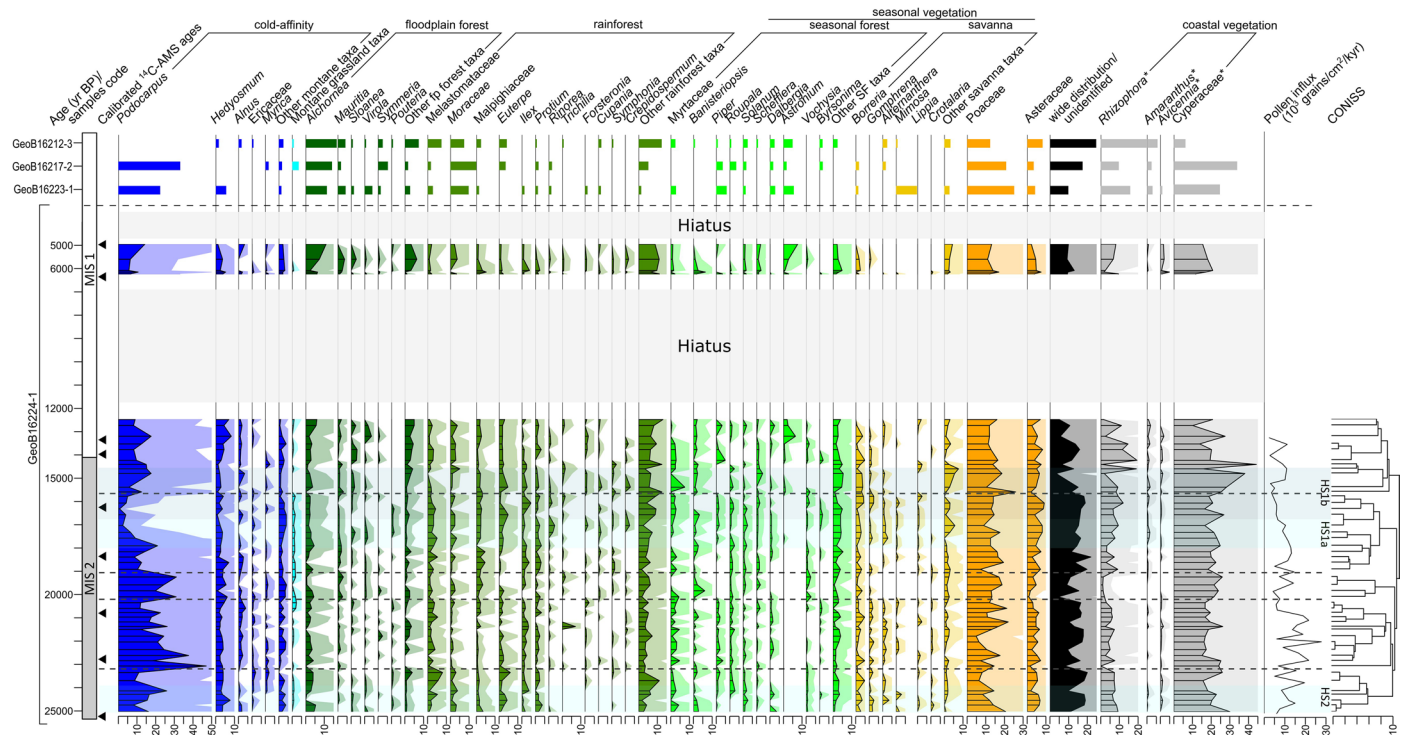
Extended Data Fig. 1 | Age model of marine sediment core GeoB16224-1. The age model is based on fifteen calibrated ^{14}C ages obtained on planktonic foraminifera⁶⁰. The calibration was performed with the Marine20 calibration curve⁶². A tie point was added at 710 cm core depth with age $46,830 \pm 470$ years

BP from the correlation of X-ray fluorescence data of core GeoB16224-1 and the El Condor stalagmite ELC-B stable oxygen isotope record (tie point)^{22,31}. The age model was produced using the 'BACON' R package⁶¹. Dashed horizontal line indicates the depositional hiatus placed at 57 cm core depth.



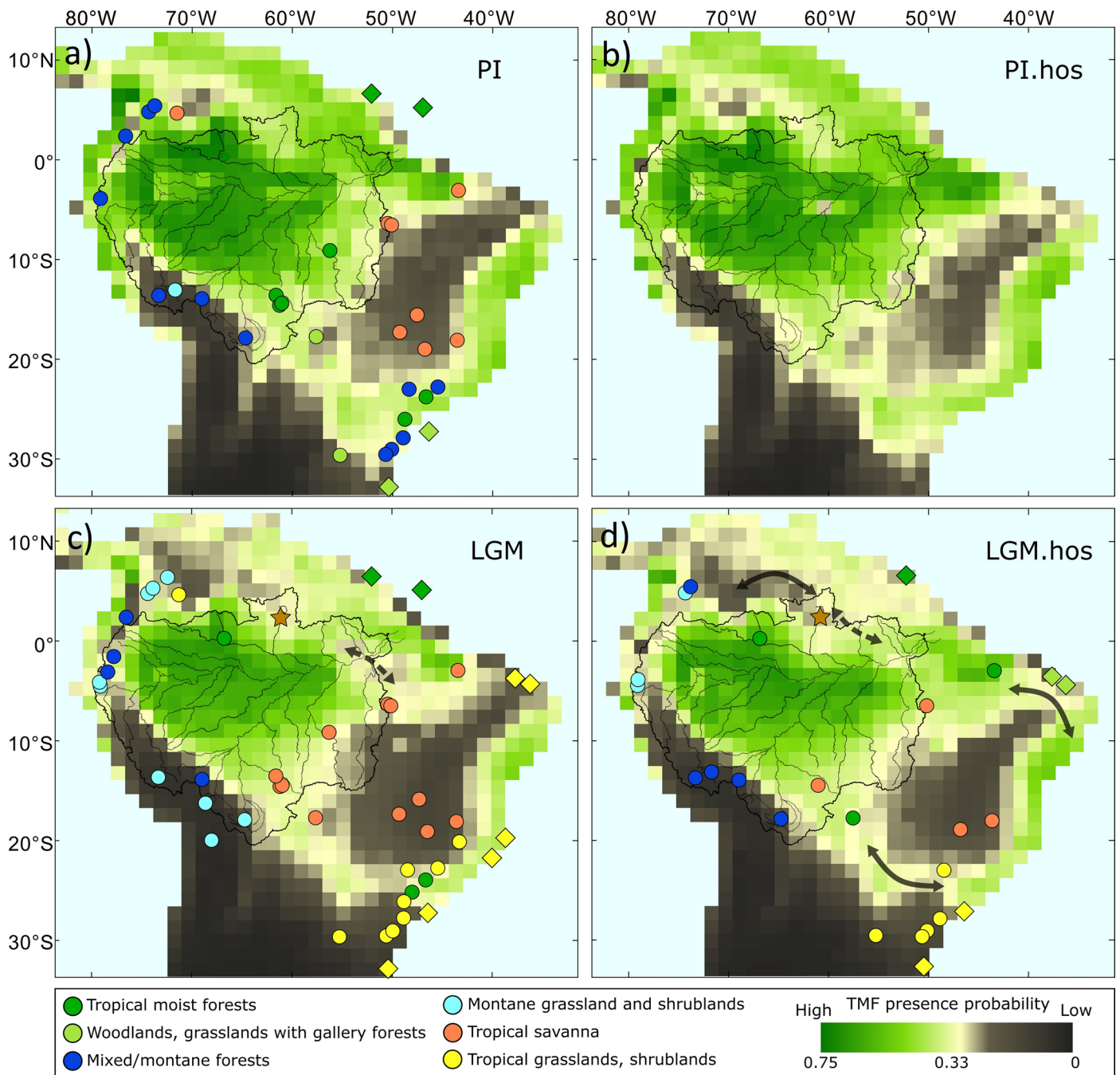
Extended Data Fig. 2 | Multivariate analysis of marine and continental Amazonian pollen signals. (a) Map with the location of all the samples used in the Correspondence analysis (CA). Marine core top (red squares), GeoB16224-1 downcore data (violet circles); modern fluvial (asterisk)²⁴, and pollen rain (crosses)²⁵ data (Supplementary Table 3). **(b)** CA after removing aquatic,

mangrove (*Rhizophora* and *Avicennia*), and interpreted coastal taxa, such as *Cyperaceae* and *Amaranthus*. **(c)** CA including mangrove and potentially coastal vegetation taxa. For both CA, we removed singletons and taxa with less than 5% abundance, *Cecropia* and aquatic taxa.



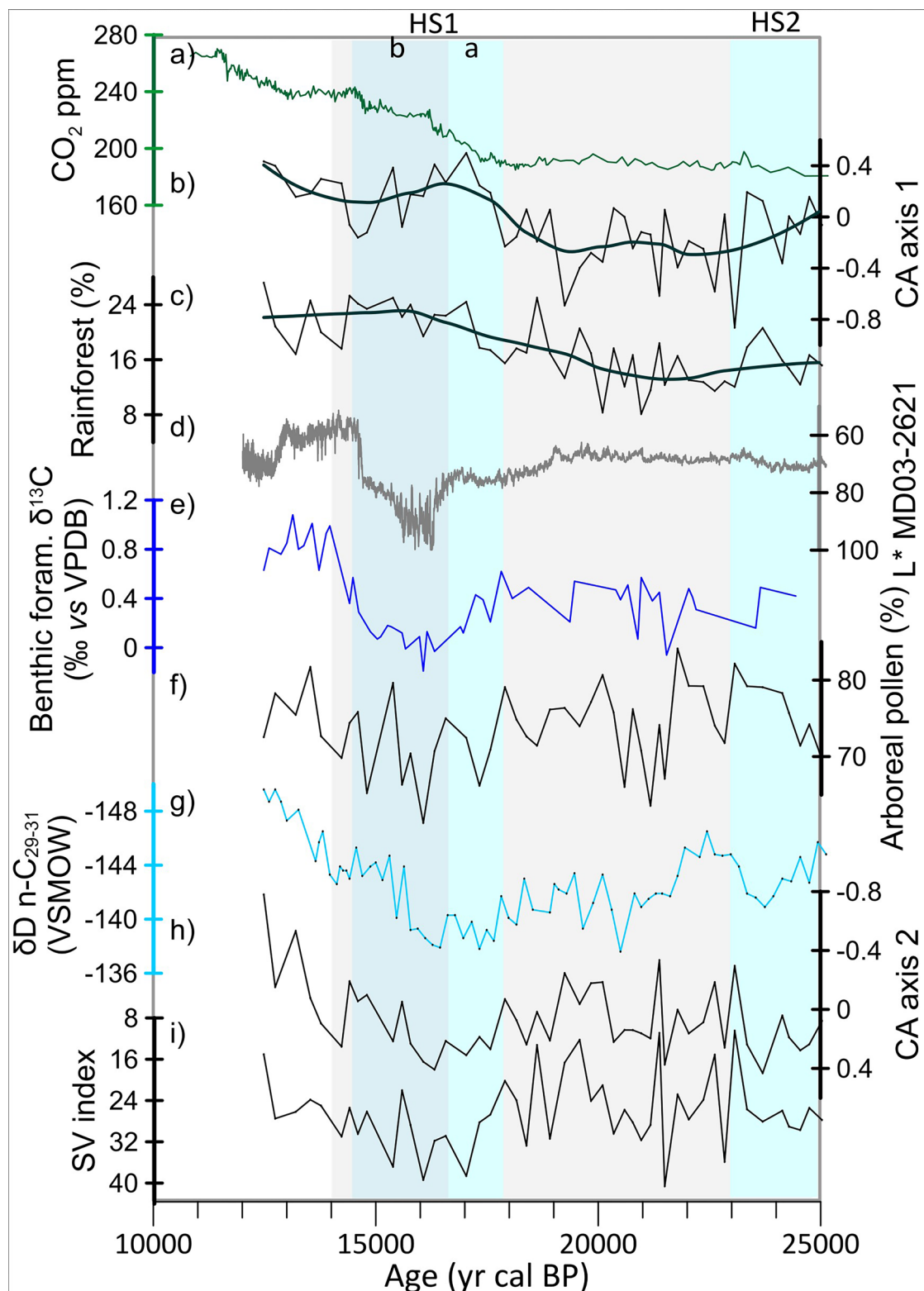
Extended Data Fig. 3 | Pollen diagram from core GeoB16224-1, and core-top samples GeoB16212-3, GeoB16217-2, and GeoB16223-1. The values are given in relative abundance calculated after excluding taxa attributed to coastal vegetation (*) (Supplementary Table 4). CONISS analysis is based on the Bray-Curtis distance of square root-transformed pollen relative abundances,

excluding coastal vegetation and taxa with less than 2% occurrence in the total sum of samples. Data from marine core GeoB16224-1 spans the interval from ca. 25,000 to 5,000 yr BP. Pollen curves exaggeration: 10 \times . Blue bands delimit the Heinrich stadials 1 (subdivided in HS1a and HS1b) and 2 (HS2). Dashed lines represent main pollen zones according to the CONISS analysis.



Extended Data Fig. 4 | Predicted suitability of tropical moist forest (TMF) over South America for different scenarios. (a) Pre-industrial (PI); (b) pre-industrial with an Atlantic meridional overturning circulation (AMOC) slowdown (PI.hos); (c) Last Glacial Maximum (LGM); (d) LGM with an AMOC slowdown, simulating Heinrich stadial 1 (LGM.hos). AMOC flow rate: (a) 18 Sv, (b) 9 Sv, (c) 12 Sv, and (d) 6 Sv. Arrows in (c) and (d) indicate potential migration routes either by the continuous (continuous arrows) or stepwise (dashed arrows) connection of forests or savannas that allowed biotic exchange and gene flow. Time-slice

averaged pollen records are indicated by circles (continental records) and diamonds (marine records) with colours representing the interpreted dominant vegetation at each site. The brown star in panels (c) and (d) indicate open vegetation or absence of vegetation cover based on sedimentary proxies. A list of the depicted records can be found in Supplementary Table 2. The value of 10th percentile training presence logistic threshold, 0.33, represents the threshold in which values equal to or higher are considered to represent suitable habitats.



Extended Data Fig. 5 | Environmental data for the last 25,000 years in the region. (a) Atmospheric CO_2 concentrations (ppm)³⁵. **(b)** Reflectance from a marine sediment record from Cariaco basin. Inverted Y axis, with lower (higher) values associated to more (less) precipitation in the northern South America – northern (southern) position of the Intertropical Convergence Zone¹⁹. **(c-i)** GeoB16224-1 data:

(c) Rainforests percentage. **(d)** Correspondence analysis (CA) axis 1 – positive values are driven by warm-affinity taxa. **(e)** Benthic foraminiferal stable carbon isotopes ($\delta^{13}\text{C}$)³⁶. **(f)** Arboreal pollen (%). **(g)** Plan-wax $\delta\text{D n-C}_{29-31}$ ²² – more negative values indicate higher precipitation. **(h)** CA axis 2 – positive values are driven mostly by dry-affinity taxa; **(i)** Seasonal vegetation index.